PAPER

Check for updates

Chemical insights into electrophilic fluorination of SnO₂ for photoelectrochemical applications†

Gaurav Bahuguna, [ID] ‡ Mohit Verma [ID] ‡ and Ritu Gupta [ID] *

Recently, there has been substantial interest in the fluorination of nanomaterials-based thin films used in various optoelectronic devices for optimum charge transport across semiconducting layers. The discovery of electrophilic fluorinating agents such as Selectfluor® (F-TEDA) has led to the development of novel methods for fluorination of metal oxides such as tin oxide (SnO_2) in this work. Herein, we elucidate the fluorination of SnO_2 thin films using X-ray photoelectron spectroscopy (XPS) depth profiling. The interaction of the F-TEDA molecule with the SnO_2 surface occurs *via* N−F bonds. Fluorine is found to occupy interstices and substitutional sites in the SnO_2 lattice. The interstitial fluorine (1.21 at%) decays off by a depth of 61 nm in the SnO_2 film. The substitutional fluorine (1.28 at%) in SnO_2 results in remarkable changes in its electronic structure due to the lowering of oxygen defects by ∼80%. The electrical properties of the F−SnO_2 film is examined by impedance spectroscopy analysis. F−SnO_2 exhibits an increase in electrical conductivity by ∼1−2 orders of magnitude and an increase in electron density by ∼65%, making it suitable as a charge transport layer in photoelectrochemical cells (PECs). The PEC in aqueous medium at neutral pH with F−SnO_2 as the charge transport layer shows ∼81% increase in the photocurrent density (at 1.6 V *versus* RHE) and decrease in charge transfer resistance by ∼36%. Thus, the efficient transport of photogenerated charge carriers is observed in PECs with minimal recombination losses for the fluorinated SnO_2 films. This study helps in understanding the role of defect passivation *via* single-step fluorination of metal-oxide for charge transport layers which can be extended to perovskite solar cells in the future.

1 Introduction

Photoelectrochemical cells (PECs) are among the most reliable approaches for renewable and sustainable energy sources.[1] However, their commercialization is still a challenge due to the associated high development costs with low power conversion efficiencies.[2] The efficiency of photoelectrode materials in PECs depends on the light absorption coefficient, conductivity, stability, surface chemical reaction rate, and charge transport across the interfaces.[3,4] Various metal oxides such as TiO_2,[5] ZnO,[6] SnO_2,[7] CdS,[8] WO_3,[9] Fe_2O_3,[10] and $BiVO_4$[11] have been explored as the photoanode material in PECs. Still, the experimentally achieved efficiency is far below that predicted by theoretical calculations.[12] Hybrid electrodes are usually fabricated by combining small and wide bandgap materials to enhance their light absorption coefficient and electron transfer efficiency. Thus, designing a photoelectrode with suitable properties is a crucial aspect for overall PEC device performance.

The n-type semiconductor SnO_2 exhibits a wide bandgap (3.6 eV) with high electron mobility, low cost, non-toxicity, high electron transfer efficiency, and high intrinsic stability.[13] It has been used as an electron transport layer in recently explored perovskite solar cells.[14–17] SnO_2 can be sensitized with different low bandgap semiconducting materials for enhancing the overall light absorption coefficient of the photoelectrode;[18,19] however, the overall performance of the hybrid electrode is limited due to the intrinsic properties of SnO_2.[20,21] Oxygen defects in SnO_2 act as trap states and affect the charge transfer process.[22] There have been numerous literature efforts to fabricate defect-free SnO_2 films with enhanced charge transport efficiency by surface passivation using fullerene,[23] phosphates,[24] and trifluoroethanol,[25] and *in situ* elemental doping with elements such as Cl,[26] P,[27] B,[28] and N.[29] Wang *et al.* observed a decrease in the bandgap and Fermi level due to chemisorbed fullerene on the SnO_2 surface, leading to a decrease in defects and enhancement in electron mobility at the interface.[23] Jiang *et al.* passivated the SnO_2 surface using 7.4 at% phosphoric acid and observed a ∼53% decrease in the surface trap states and enhanced electron mobility.[24] Luan *et al.* modified SnO_2 with trifluoroethanol for improving electron mobility.[25] Similarly, chlorine-passivated SnO_2 QDs led to an increase in the Fermi level and reduction of interfacial defects.[26] Tan *et al.* developed

Department of Chemistry, Indian Institute of Technology Jodhpur, Jodhpur, Rajasthan-342037, India. E-mail: ritu@iitj.ac.in

† Electronic supplementary information (ESI) available. See DOI: 10.1039/d1ta02560k

‡ Both authors contributed equally.

This journal is © The Royal Society of Chemistry 2021

J. Mater. Chem. A, 2021, **9**, 19965–19974 | **19965**

a contact-passivation strategy by capping TiO_2 with chlorine to minimize defects and charge recombination.[30] Mokaripoor et al. fabricated transparent conducting SnO_2 films by co-doping phosphorus and fluorine, leading to a decrease in the bandgap and high electrical conductivity.[27] In an interesting study, Zhang et al. reported a decrease in the electron mobility, while, contrarily, the carrier concentration increases on increasing the boron doping (0–5 wt%).[28]

Fluorine-doped SnO_2 with metallic conductivity and high transparency is well known in optoelectronic applications as a transparent conducting oxide (TCO);[31] however, its role as a charge transport layer in photoelectrochemical cells is not well explored. Surface fluorination of SnO_2 can be controlled and tuned to reduce oxygen defects and enhance the conductivity, transparency, and electron mobility for an efficient charge transport layer.[27] The type of fluorine doping (substitutional/interstitial) in the SnO_2 lattice has a direct influence on its optoelectronic properties. Substitutional F-doping is known to enhance the mobility of SnO_2; however, interstitial doping can have detrimental effects due to self-compensation.[32] Hence, the type of doping and its extent are crucial parameters for the fabrication of fluorinated SnO_2. In this study, we use F-TEDA (Selectfluor®) as a fluorinating precursor. It is a commercially available, stable solid and a non-hazardous source of reactive fluorine. The precursor with the N–F bond releases electrophilic fluorine species in the solution at low temperature with potential to readily react with the metal oxides. Other solution processes include corrosive precursors such as HF[33] and NH_4F[34] that etch the oxides or even the less reactive NaF precursor,[35] which acts as a growth-directing agent, and the fluorine content is non-traceable in the SnO_2 lattice.[36,37] The F-TEDA precursor provides a highly reactive yet safe to use method, unlike direct fluorination by fluorine-containing gases such as $(Ar:F_2)$,[38] SF_6,[39] and CF_4.[40] Conventionally, fluorinated thin films are prepared by an extensive process involving DC magnetron sputtering or spray pyrolysis of metal fluorides.[41,42] Thus, the F-TEDA-based route is advantageous as it provides a convenient, less expensive, and instrumentation-free, solution processing method for fluorination of SnO_2 films. In previous reports, by using F-TEDA as an electrophilic fluorine precursor, we have developed a recipe for fluorination of various nanomaterials, including SnO_2 for the fabrication of gas sensors and energy storage devices.[43,44] However, a clear understanding of the fluorination mechanism and its influence on the band structure is still missing in the literature. Herein, an in-depth study is carried out for understanding the fluorination process using XPS depth profiling and its influence on electrical properties, surface oxygen defects, trap states, and electronic energy levels by impedance and UPS spectroscopic studies. The role of fluorinated SnO_2 as a charge transport layer is elucidated for the overall improvement of CdS–TiO_2-based photoelectrochemical cells.

2 Experimental section

(a) Fabrication of F–SnO_2 films

The SnO_2 film was prepared on pre-cleaned FTO substrates by spin-coating (1 M) $SnCl_2$ (tin(II) chloride, Rankem) solution in ethanol and rapidly annealing for 15 minutes at 500 °C. Fluorination was carried out by treating the SnO_2 films in Selectfluor® (F-TEDA, 1-chloromethyl-4-fluoro-1,4-diazoniabicyclo [2.2.2] octane bis(tetrafluoroborate), Sigma-Aldrich) solution (0.05 M) in acetonitrile at 60 °C for one hour, followed by washing the substrate with acetonitrile and heating at 150 °C for 15 min, resulting in the formation of the F–SnO_2 film.

(b) Fabrication of the PEC electrode using CdS–TiO_2 as the sensitizer (S*)

The CdS–TiO_2 composite paint was prepared by pseudo-SILAR (Successive Ionic Layer Adsorption and Reaction) following a literature method.[45] Briefly, TiO_2 slurry (0.5 g in 1 mL) was prepared in a water and methanol (3 : 1) mixture. 2 mL of $CdSO_4$ (0.1 M in water : methanol, 1 : 1) and 2 mL Na_2S (0.1 M in water : methanol, 1 : 1) were added sequentially to the TiO_2 slurry and mixed for 30 s. The mixture was centrifuged at 7000 rpm, and the supernatant was discarded. By eight such repeated cycles, CdS–TiO_2 powder was obtained and redispersed in tert-butyl alcohol : water (2 : 1) to form CdS–TiO_2 paint. Finally, the CdS–TiO_2 paint was applied on F–SnO_2 and SnO_2 coated FTO substrates (1 × 1 cm², ∼10 Ω sq⁻¹) by the doctor-blade method to form micron-thick films after annealing at 200 °C under nitrogen for 60 minutes.

(c) Characterization

X-ray photoelectron spectroscopy (XPS) and ultraviolet photoelectron spectroscopy (UPS) measurements were performed on a Thermo Scientific NEXSA surface analysis system. High-resolution XPS depth profiling was performed employing X-ray operated at 12 kV and 72 W and an experimentally determined sputter rate of approximately 0.4–0.5 nm s⁻¹ collected at 150 eV pass energy. Carbon correction in the XPS data is performed relative to the standard C 1s peak at 284.6 eV. The peak fitting and baseline corrections are performed using Fityk software. UPS measurements were performed with a He1 (21.2 eV) source for studying the changes in the band position, electronic states of Sn and O, and their defect states. The band positions in the film were calculated using the following equations:[46,47]

$$E_F = E_{\text{cut-off}} - 21.2 \text{ eV (emission energy from He irradiation)} \quad (1)$$

$$VB = hv - (E_{\text{cutoff}} - E_{\text{onset}}) \quad (2)$$

$$CB = VB + E_g \quad (3)$$

where $E_{\text{cut-off}}$ and E_{onset} are the secondary electron cut-off and valence band edge obtained by extrapolation in the higher and lower energy regions in the UPS spectrum, E_F is the Fermi energy level, VB is the valence band maxima, CB is the conduction band minima, and E_g is the bandgap. UV-visible spectroscopy (Varian Cary 4000) measurements were performed in the range of 200–800 nm. The bandgap, E_g, of SnO_2 and F–SnO_2 films was calculated using the Tauc plot equation: $(\alpha hv)^2 = A(hv - E_g)$,[47] where α is the absorption coefficient, hv is

19966 | J. Mater. Chem. A, 2021, **9**, 19965–19974

This journal is © The Royal Society of Chemistry 2021

the photon energy, A is a constant, and E_g is obtained by the linear extrapolation. Temperature-dependent conductivity was measured using liquid nitrogen on a temperature-controlled Linkam stage (THMS600). XRD (D8, Bruker) measurement was performed using Cu Kα radiation (λ = 1.5418 Å). FESEM imaging and EDX analysis (Tescan-Mira 3 LMH) were performed to analyse the surface morphology and elemental composition. Photoluminescence (PL) measurement of the SnO_2 and $F–SnO_2$ films was performed at an excitation wavelength of 325 nm using a Jasco spectrophotometer. Electron paramagnetic resonance (EPR) spectra were recorded from powder samples (scrapped off from the solid film) on a JES-FA200 ESR spectrometer with an X-band frequency of 9.48 Hz at room temperature. The ohmic contacts are made using silver paint across a gap of ∼2 mm in SnO_2 and $F–SnO_2$ films for electrical measurements. AC impedance spectroscopy measurements were performed at 0.4 V in the frequency range of 1 kHz to 10 MHz using an Ivium Stat (Netherlands) electrochemical workstation at different temperatures using a temperature-controlled Linkam stage (THMS600). The activation energy was calculated from the Arrhenius plot using the equation[48] $\tau = \tau_o \exp(-E_a/K_B T)$, where τ_o is the pre-exponential factor, E_a is the activation energy, K_B is the Boltzmann constant and T is the temperature. Photoelectrochemical measurements of the fabricated electrodes were carried out on an electrochemical workstation (CHI 660E, USA) in a typical three-electrode geometry with a platinum wire as a counter electrode and Ag/AgCl as a reference electrode in 0.5 M aqueous Na_2SO_4 as the neutral electrolyte. The photoresponse was analysed using a xenon lamp with a light intensity of 20 mW cm^{-2}. Mott–Schottky analysis was performed in the dark using 0.5 M Na_2SO_4 solution at a frequency of 1 kHz. Electrochemical impedance spectroscopy (EIS) was performed in the range 0.1 Hz to 1 MHz at open circuit potential. The EIS parameters were calculated by fitting using EIS spectrum analyser software.

3 Results and discussion

The nanocrystalline SnO_2 films prepared by spin coating of the precursor solution were used for developing the fluorination process in the study. Fig. 1a shows the fluorination method for SnO_2 thin films of thickness ∼240 nm using F-TEDA as an electrophilic fluorine precursor (ESI Fig. S1†). Briefly, the SnO_2 film is dipped in F-TEDA solution (0.05 M) at 60 °C for 1 h, rinsed with deionized water gently for cleaning and removing the excess precursor sticking on the SnO_2 surface, and finally heated at 150 °C for 15 min to form the $F–SnO_2$ film. The doping of fluorine in the SnO_2 lattice is demonstrated by the schematic in Fig. 1a. There was no significant change in the morphology of SnO_2 upon fluorination (ESI, Fig. S2†). In any case, the post-
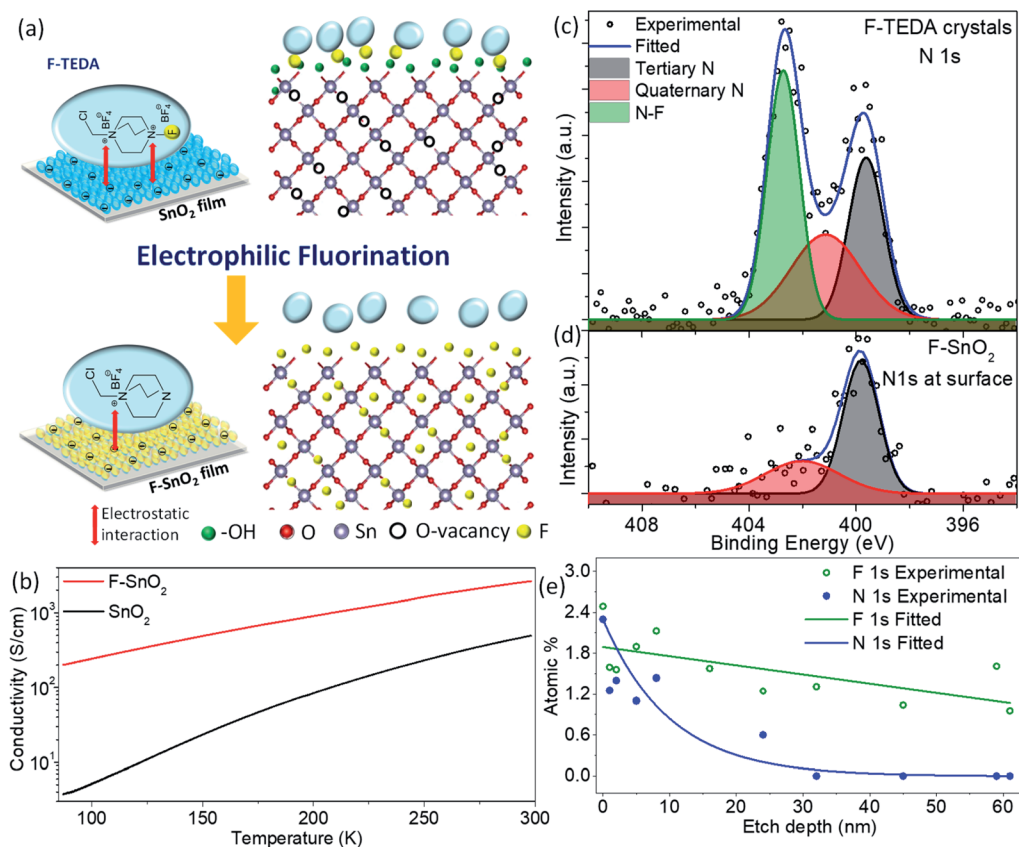

Fig. 1 (a) Schematic demonstrating the fluorination process of the SnO_2 film using the F-TEDA molecule as the fluorinating precursor. (b) Temperature-dependent conductivity of SnO_2 and $F–SnO_2$ films. (c and d) Deconvoluted N 1s HR-XPS spectra of the F-TEDA precursor compared with the $F–SnO_2$ film. (e) Atomic % distribution *versus* etch depth for N 1s and F 1s across the $F–SnO_2$ film.

synthetic method for fluorination does not affect the nucleation process of SnO_2 and the amount of fluorine incorporated is far too less to have any effect on the crystal lattice. The XRD pattern (Fig. S3†) shows a slight broadening of peaks upon fluorination due to the decrease in crystallite size by ~6.6% (Table S1†).[49] SEM-EDX mapping shows a uniform distribution of fluorine (~3.35 at%) in the F–SnO_2 film (Fig. S4†). Interestingly, the fluorinated SnO_2 exhibits a reduction in sheet resistance by an order of magnitude (from ~0.1 MΩ sq^{-1} to ~5 kΩ sq^{-1}), confirming fluorination. The increase in conductivity is expected since fluorine atoms act as donors by supplying free electrons at oxygen vacancies in SnO_2 on fluorination.[41] The low-temperature conductivity measurements show more than an order of increase in conductivity for F–SnO_2 due to reduced scattering of charge carriers (Fig. 1b).

The high-resolution N 1s spectra of the F-TEDA molecule and the fluorinated SnO_2 surface were examined as the N–F bond plays a major role in the fluorination process (Fig. 1c and d). The deconvoluted N 1s spectra of the F-TEDA precursor exhibit three peaks, quaternary-N (401.14 eV), tertiary-N (399.64 eV), and the third corresponding to the N–F bond (402.73 eV), as expected based on the structure of the molecule (Fig. 1c). Interestingly, the N 1s spectrum from the SnO_2 originating due to the residual molecule bound to the film surface could be deconvoluted to two peaks only. The disappearance of the third

peak at 402.73 eV indicates the structural changes after the release of fluorine species upon N–F bond dissociation (Fig. 1d). The N–F bond of F-TEDA is known to result in "F$^+$" species that are highly reactive.[50] This necessitates further probing of the SnO_2 surface to explore various questions about whether the F-TEDA molecule adsorbs on the surface and releases fluorine to the SnO_2 film or not. If in case fluorine diffuses inside the SnO_2 film, further in-depth analysis of nitrogen and fluorine signals from the N–F bond is required for quantification. As shown in Fig. 1e, the nitrogen signal (for tertiary and quaternary nitrogen) falls exponentially and drops to the background value by an etch depth of ~32 nm (ESI, Fig. S5†), indicating that the molecule is only absorbed on the surface and not incorporated into the SnO_2 lattice. Moreover, the C 1s signal decreases in the same trend as N 1s (Fig. S6†), and it can be inferred that the signal originates from the surface-bound residual F-TEDA molecule after the release of fluorine species. The cationic part of the residual F-TEDA molecule is probably held to the negatively charged SnO_2 surface with weak electrostatic interactions (schematic, Fig. 1a) as is observed for polyelectrolyte cations[51] and polar dyes[52] in the literature. However, a fluorine content of ~2.49 at% on the surface falls off steadily to ~1 at%, as analysed at a depth of 61 nm in the SnO_2 lattice.

The XPS sputtering depth profile is obtained for understanding the chemical state and atomic concentration of
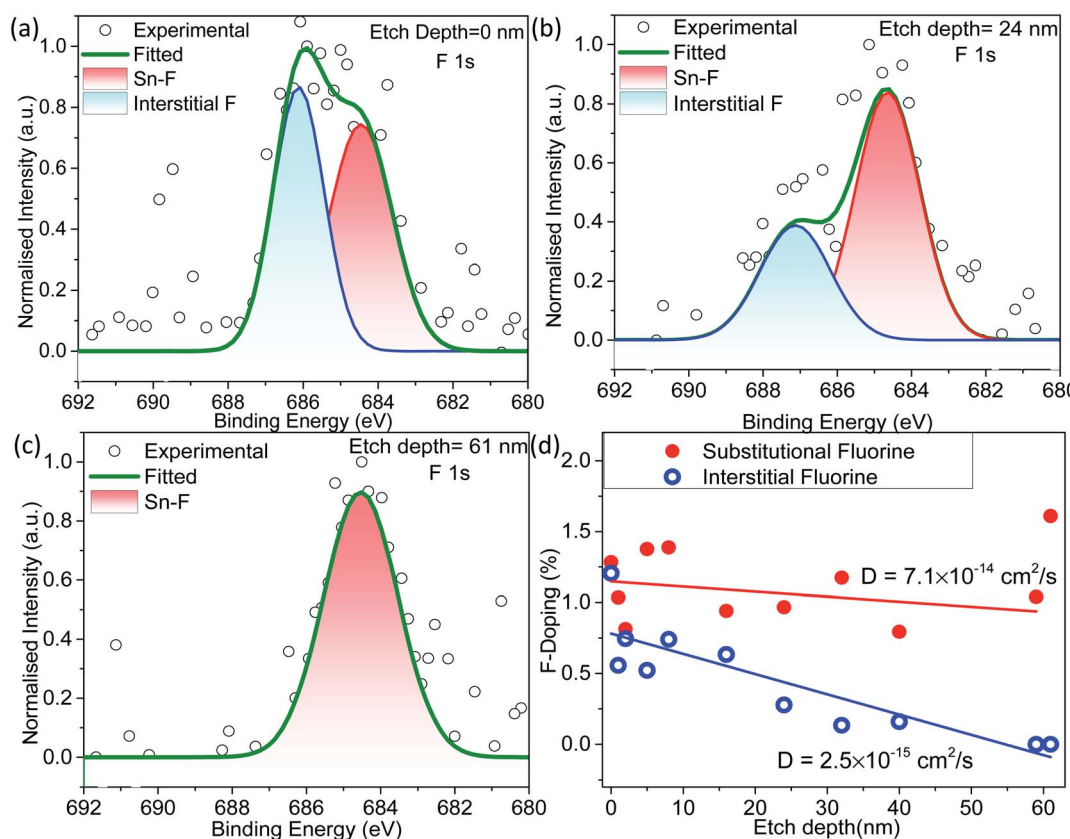

Fig. 2 Deconvoluted XPS spectra of F 1s from different etching depths of (a) 0 nm (at the surface), (b) 24 nm, and (c) 61 nm of F–SnO_2, respectively. Spectra (a–c) are normalized to the maximum intensity. (d) Variation in substitutional and interstitial fluorine percentage present in the F–SnO_2 lattice.

19968 | J. Mater. Chem. A, 2021, 9, 19965–19974

This journal is © The Royal Society of Chemistry 2021

fluorine present in F–SnO$_2$ films. A broad peak of F 1s obtained at 684.5 eV is associated with Sn–F bonding (Fig. 2a). The solution-based fluorination process occurs throughout the depth of the SnO$_2$ film. However, fluorination is generally assumed to be substitutional, involving the replacement of the oxygen vacancy by fluorine. Deconvolution of the F 1s peak is not only crucial for elucidating the nature of fluorination but also disentangling the contribution of substitutional and interstitial doping taking place in the SnO$_2$ film. The F atom residing in the interstitial site occurs at higher binding energy than substitutional fluorine.[32] In Fig. 2a, the F 1s peak for substitutional doping at 684.5 eV could be easily distinguished from the interstitial peak at 686.5 eV by the surface scan profile. The F 1s peak at different etch depths of 24 nm and 61 nm is shown in Fig. 2b and c, respectively, for highlighting the differences in fluorine distribution with respect to the depth of the film. It is interesting to relate the decrease in the amount of total fluorine to the interstitial fluorine since there is no significant change in the percentage of substitutional fluorine throughout the depth of the film examined (ESI, Fig. S7†). It can be clearly observed that substitutional doping (1.28 at%) remains nearly constant while interstitial doping (1.21 at%) decreases gradually with repeated sputtering cycles and falls off

by 61 nm due to less diffusion of fluorine across the depth of the film, indicating that the process is surface-dominated (Fig. 2d). The diffusion length (L) of substitutional and interstitial fluorine in the F–SnO$_2$ lattice is estimated by extrapolation of the depth profile data and the diffusion coefficient, D, is calculated using the relation $L = \sqrt{4Dt}$, where t is the reaction treatment time for fluorine diffusion to take place.[53] Interestingly, substitutional fluorination exhibits one order higher diffusion coefficient of 7.1×10^{-14} cm^2 s^{-1} than the interstitial one (2.5×10^{-15} cm^2 s^{-1}), which is understandable due to the energetically unfavourable interstitial doping in the compact rutile SnO$_2$ structure.[54,55]

As seen from the line depth profile in Fig. 3a, Sn and O atoms are uniformly distributed with a constant Sn/O ratio of 0.51. The high-resolution Sn 3d$_{5/2}$ spectra give information about the defects present in the pristine and fluorinated SnO$_2$ (Fig. 3b and c). Sn 3d$_{5/2}$ can be deconvoluted into two peaks at ∼486 eV (Sn^{2+}) and ∼487 eV (Sn^{4+}) in the SnO$_2$ lattice.[40] Sn^{2+} species in the SnO$_2$ lattice are formed due to the insufficient oxygen component, thus acting as oxygen defects in the lattice.[56] Pristine SnO$_2$ is composed of a higher percentage of Sn^{2+} (∼25.6%) which is decreased to ∼3.9% in the F–SnO$_2$ film. Moreover, there is an appearance of a third peak at 487.5 eV (Fig. 3c),
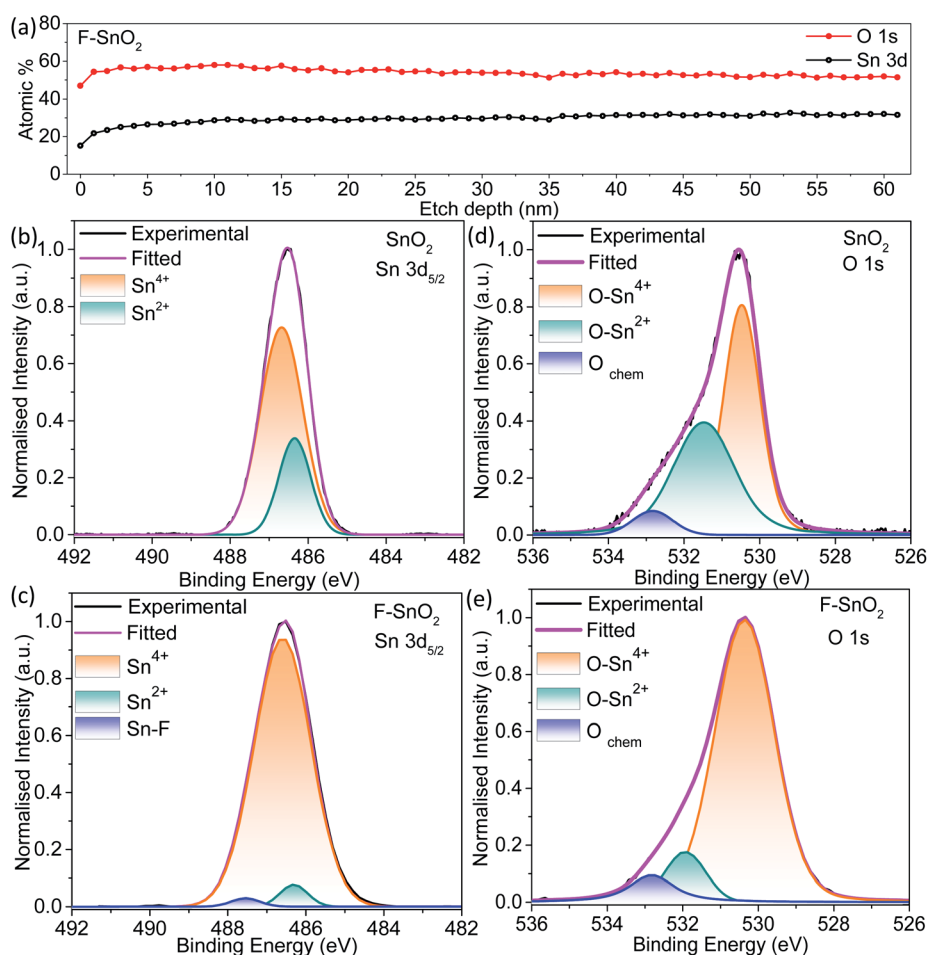

Fig. 3 (a) Atomic percentages of Sn 3d and O 1s calculated from XPS of the F−SnO$_2$ film at different depths. Deconvoluted XPS spectra of (b and c) Sn 3d$_{5/2}$ and (d and e) O 1s of pristine SnO$_2$ and F−SnO$_2$, respectively.

which can be assigned to the Sn–F bond based on the literature.[57] To further quantify the oxygen defects present in the pristine and F–SnO$_2$ films, O 1s spectra of SnO$_2$ and F–SnO$_2$ are deconvoluted into three peaks, as shown in Fig. 3d and e. The first peak at ~530 eV is related to the O in the SnO$_2$ lattice (O–Sn^{4+}) and the second peak at ~533 eV is due to the adsorbed O species. The third peak at ~531 eV is associated with the non-stoichiometric oxygen defects (O–Sn^{2+}).[24] The O 1s peak position and area under the curves for O–Sn^{2+} and O–Sn^{4+} are tabulated in Table S2.† It can be observed that the oxygen defects in pristine SnO$_2$ (17.2%) passivate and are reduced to a mere 3.4% upon fluorination (Table S2†). The lower oxygen defect ratio in F–SnO$_2$ is of significance for efficient electron transport in photoelectrochemical devices. Otherwise, these oxygen defects act as trap states and enhance the recombination of photogenerated charge carriers. PL and EPR studies were performed additionally to account for the oxygen defects in SnO$_2$ before and after fluorination. In the PL spectra (Fig. S8†), F–SnO$_2$ shows a significant decrease in the peaks at ~410 nm and ~463 nm, which is attributed to fluorine-mediated passivation of oxygen defects at mid band trap states (V_o^{+} and V_o^{0}). EPR shows a broad signal for SnO$_2$ that disappears in F–SnO$_2$ due to the reduction in oxygen defects (Fig. S9†).

The DC and AC electrical properties of the SnO$_2$ and F–SnO$_2$ films are investigated to understand the role of fluorination. Fig. 4a shows symmetrical ohmic I–V characteristics with ~2 order increase in current upon fluorination. The Nyquist plots show a single semi-circle corresponding to the granular thin films. The impedance data is fitted using an RC equivalent circuit with series contact resistance, R_C (inset, Fig. 4b and c). The resistance R_B represents the bulk resistance of the nano-crystalline film while capacitance from grain boundaries is replaced with a constant phase element, CPE, for fitting.[58,59] The parameters are tabulated in ESI, Table S3.† The SnO$_2$ film fits well to the equivalent circuit, while F–SnO$_2$ exhibits a distorted semicircle in the high-frequency region, thus deviating slightly from the fitted curve. A drastic reduction in bulk resistance value of F–SnO$_2$ (7.04 kΩ) in comparison to that of the SnO$_2$ film (1598.8 kΩ) is observed upon fluorination similar to the changes observed in I–V measurements. The bulk resistance decreases with increasing temperature at each frequency more sharply for SnO$_2$ as compared to F–SnO$_2$ due to the thermally excited conduction mechanism and increase in scattering of charge carriers (Fig. S10†). In Fig. 4d, F–SnO$_2$ shows higher capacitance than SnO$_2$ over a wide frequency range without exhibiting any plateau region. The remarkable enhancement in the capacitance in F–SnO$_2$ can be related to the increase in surface electron concentration from fluorine that effectively dominates the electrical charge transport.[60] The high-frequency plateau in capacitance for SnO$_2$ is attributed to the extrinsic contributions from grain boundaries.[61] Furthermore, a two-order lower real impedance (Z′) reaffirms the high AC conductivity of F–SnO$_2$ films (Fig. 4e). In F–SnO$_2$, Z′ is purely resistive in nature over a wide frequency region as the barrier to capacitive grain boundaries and other defects is diminished by the increase in electronic charge concentration from fluorine, thus releasing the space charge that otherwise is present in SnO$_2$ films.[58] The imaginary impedance (−Z″) versus frequency gives information of the electrical field relaxation time (τ) at the maximum frequency (f_{max}). The −Z″ attains peak maximum at much higher frequency for F–SnO$_2$ with ultrafast relaxation (0.27 μs) of charge carriers, resulting in high mobility and AC conductivity (Fig. 4e). With increasing temperature, the SnO$_2$ film shows asymmetric broadening and shifting of the peaks with a decrease in −Z″, indicating a temperature-dependent electrical relaxation process with the spread of relaxation times due to trap states, vacancies, and oxygen defects (Fig. S11†). Interestingly, the passivation of such defects in F–SnO$_2$ minimizes the shift in −Z″$_{max}$ with increasing temperature (Fig. S12†). The activation energy (E_a) calculation from
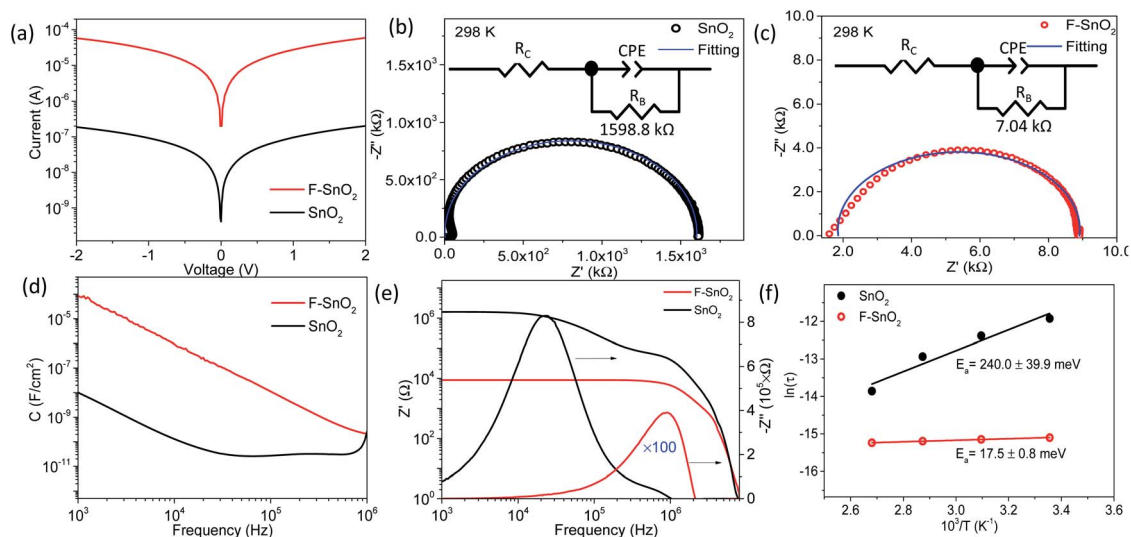

Fig. 4 (a) I–V characteristics and (b and c) Nyquist plots of SnO$_2$ and F–SnO$_2$ films, respectively. Inset in (b and c) shows the equivalent circuit diagram used for fitting. (d) Capacitance versus frequency. (e) Real part (Z′) and imaginary part (−Z″) of impedance as a function of frequency for SnO$_2$ and F–SnO$_2$ films. (f) Arrhenius plot of ln(τ) versus 1/T (K^{-1}) obtained from impedance analysis at different temperatures.

19970 | J. Mater. Chem. A, 2021, **9**, 19965–19974

This journal is © The Royal Society of Chemistry 2021

temperature-dependent imaginary impedance shows a dramatic reduction in the E_a value for the SnO$_2$ film (240 meV) to 17.5 meV in F–SnO$_2$ (Fig. 4f). These results are appreciable since the concentration of fluorine influences the electron density, thus increasing the conductivity and, consequently, activation energy decreases on fluorination.

The SnO$_2$ and F–SnO$_2$ films show transmittance > 80% in the visible range (Fig. 5a, inset), making these suitable for optoelectronic device application. The bandgap of the F–SnO$_2$ film is ~3.71 eV, slightly higher than that of the SnO$_2$ film (~3.67 eV). The increase in the bandgap upon fluorination is due the filling of low-lying energy levels in the conduction band of F–SnO$_2$, thus widening the bandgap. This is the Burstein–Moss effect well-known in the literature for transparent conducting oxides

including fluorinated tin oxide.[41] The electronic structure was studied by analysing the density of states below E_F of pristine and F–SnO$_2$ films (Fig. 5b). The band structures of SnO$_2$ and F–SnO$_2$ films differ significantly, as evident from the secondary electron cut-off (inset, left in Fig. 5b) and valence-edge spectra (inset, right in Fig. 5b). Upon fluorination, the VB shifts to lower energy, and E_F is raised relative to the SnO$_2$ film. The valence band edge (E_{onset}) is shifted to 3.9 eV in F–SnO$_2$ with respect to the SnO$_2$ (3.6 eV) film. The slope at the valence edge (lower cut-off BE) gives information about the oxygen defects (Sn^{2+} type species) in the SnO$_2$ film, forming 5s and 5p hybrid states.[62] The changes in the electronic density (reduction in slope) of the valence state upon fluorination can be attributed to substitutional doping of the SnO$_2$ lattice by fluorine (observed in XPS),
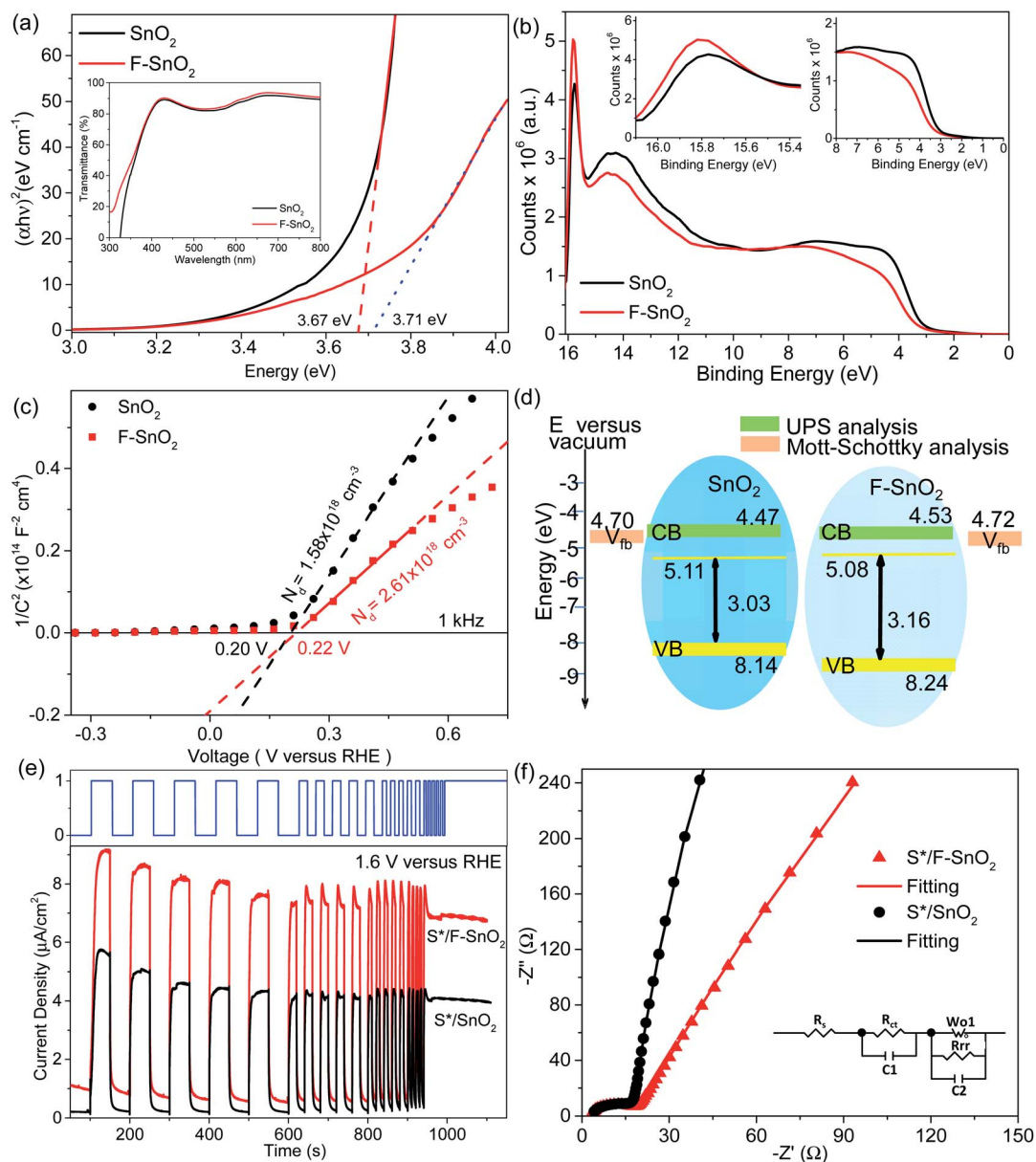

Fig. 5 (a) Tauc plot for bandgap analysis and the corresponding UV-visible spectra (inset). (b) UPS survey spectra with the inset showing the magnified view of valence band spectra. (c) Mott–Schottky plots and (d) energy band diagram of pristine SnO$_2$ and F–SnO$_2$ films. (e) J–t measurements (at 1.6 V *versus* RHE) and (f) Nyquist plots of S*/SnO$_2$ and S*/F–SnO$_2$. Inset in f shows the equivalent circuit.

This journal is © The Royal Society of Chemistry 2021

J. Mater. Chem. A, 2021, **9**, 19965–19974 | **19971**

which reduces the oxygen defects, thus diminishing 5s–5p hybrid states. The shifting of the VB towards lower energies in F–SnO$_2$ enhances its performance as an electron transport layer in PECs due to increased charge transport.[63]

Furthermore, to evaluate the flat band potential (V_{fb}) of the space charge region and the donor density (N_d), Mott–Schottky analysis of SnO$_2$ and F–SnO$_2$ was performed in neutral medium (0.5 M Na$_2$SO$_4$ solution) and calculated using the equation:[64]

$$\frac{1}{C^2} = \frac{2}{q\varepsilon A^2 N_d}\left(V - V_{fb} - \frac{kT}{q}\right) \qquad (4)$$

where C is the capacitance of the space charge region, q is the electric charge, ε is the dielectric constant of SnO$_2$ (9.86), N_d is the donor density, A is the surface area of the interface, V is the applied potential, and V_{fb} is the flat band potential. The Mott–Schottky plots ($1/C^2$ versus V) of SnO$_2$ and F–SnO$_2$ films show positive slopes indicating n-type semiconductor behavior (Fig. 5c). Interestingly, F–SnO$_2$ exhibits ~65% increase in donor density (N_d (F–SnO$_2$) = 2.61×10^{18} cm^{-3}) in comparison to pristine SnO$_2$ (N_d (SnO$_2$) = 1.58×10^{18} cm^{-3}). The increase in carrier concentration in F–SnO$_2$ also explains the observed increase in the Fermi level. Furthermore, a slight shift in V_{fb} for F–SnO$_2$ by 0.02 eV is in conjugation with that observed in UPS analysis. The E_F, VB, and CB energies for both pristine and F–SnO$_2$ calculated from UPS spectra (see the Experimental section for details) and Mott–Schottky plots are represented in the energy band diagram in Fig. 5d. Overall, substitutional fluorination in the SnO$_2$ film decreases the oxygen defects, increases the donor density, and shifts the bands towards lower energy that can be synergistically beneficial for enhanced electron transport in PECs with a suitable sensitizer.

The electron transport property of the pristine SnO$_2$ and F–SnO$_2$ films on the FTO substrate was experimentally tested in a PEC by depositing CdS–TiO$_2$ as a sensitizer (abbreviated as S*) following a pseudo-SILAR method. The UV-vis diffuse reflectance spectrum of CdS–TiO$_2$ (S*) is shown in ESI, Fig. S13.† The photoelectrodes are annotated as S*/SnO$_2$ and S*/F–SnO$_2$ (shown in ESI, Fig. S14†). The photoresponse curves (J–t) of S*/SnO$_2$ and S*/F–SnO$_2$ at 1.6 V versus RHE with chopped light illumination are shown in Fig. 5e. Both the electrodes exhibit a spontaneous increase and decay in current density on exposure to varying input photo-pulses of the square waveform, suggesting a rapid transfer of the photogenerated electrons from the sensitizer (S*) to the current collector. It is interesting to observe a ~81% increase in photocurrent density with the F–SnO$_2$ (~8.13 μA cm^{-2}) electrode in comparison to that with SnO$_2$ (~4.47 μA cm^{-2}). The photoresponse is even stable to continuous exposure of incident light for 150 seconds after the photo-pulse experiment. Similarly, the LSV curve at 5 mV s^{-1} for S*/F–SnO$_2$ exhibits a higher photocurrent density than S*/SnO$_2$ in the entire voltage range with a photocurrent density of 19.89 μA cm^{-2} and 7.41 μA cm^{-2}, respectively at 1.6 V versus RHE (ESI, Fig. S15†). Such a significant increase in photocurrent density is due to the enhanced electron transport at the S*/F–SnO$_2$ interface.

Electrochemical impedance spectroscopy (EIS) was performed to analyse the charge transfer processes occurring at the electrode–electrolyte interface. The Nyquist plots (Fig. 5f) under illumination conditions were fitted with the equivalent circuit (inset), and the derived values are tabulated in Table S4.† R_s is the series resistance at the interface of the photoanode material and the FTO substrate, while the parallel R_{CT} and C1 elements give the charge transfer resistance. The capacitance in the semiconducting layer and the semiconductor–electrolyte interface is characterized by a double layer capacitance (C2) and a faradaic component (a charge transfer resistance, R_{rr} and Warburg element W_o), respectively. SnO$_2$ exhibits large R_{CT} and R_{rr} values of 13.4 Ω and 10.7 kΩ, respectively, which reduces to 12.8 Ω and 6.8 kΩ for F–SnO$_2$. This enhanced charge transport in S*/F–SnO$_2$ is a result of reduced recombination at the interface due to limited defects and enhancement in the donor density of F–SnO$_2$.

In summary, the incorporation of fluorine into the SnO$_2$ lattice could be observed in two ways i.e. substitutional and interstitial. The substitutional fluorine occupies the place of oxygen in the SnO$_2$ lattice (due to the comparable size of O^{2-} and F$^-$), thus passivating the oxygen vacancies which are present as defects in the lattice.[48] On the other hand, the insertion of fluorine in the interstitial site of the SnO$_2$ lattice does not influence the oxygen defects; rather, it is known to have pernicious effects by limiting the achievable mobility of the charge carriers.[32] F–SnO$_2$ as the charge transport layer shows ~81% increase in the photocurrent density and decrease in charge transfer resistance by ~36%. This enhancement in the photocurrent density is because of the reduction in the recombination losses of charge carriers in F–SnO$_2$ films, which is expected due to the decrease in the oxygen vacancies which act as trap states for the charge carrier and increase in the electrical conductivity upon substitutional fluorination. The shifting of the valence band towards lower energies in F–SnO$_2$ further limits charge recombination and enhances the charge transport at the sensitizer–SnO$_2$ interface.

4 Conclusion

In conclusion, we have successfully doped fluorine into SnO$_2$ films using F-TEDA as a fluorinating precursor by the solution processing method. The fluorinated SnO$_2$ films are studied using highly powerful surface-sensitive techniques (XPS and UPS) for understanding the effect of fluorine on the composition and electronic band structure of SnO$_2$. The nature of fluorine doping (~2.49 at%) is examined across the depth of the SnO$_2$ film. Apart from substitutional fluorine, the surface of the F–SnO$_2$ film is enriched with interstitial fluorine (1.21 at%) that decays completely by 61 nm depth. The incorporation of fluorine passivates the surface defects in the SnO$_2$ film, increases the electrical conductivity by two orders of magnitude and drastically reduces the activation energy to 17.5 meV. The F–SnO$_2$ layer enhances the electron transport from the photoactive CdS–TiO$_2$ sensitizer to the electrode, resulting in a significantly suppressed electron accumulation and excellent PEC performance. Fluorination is a promising strategy towards defect passivation in charge transport layers and is of significant importance in optoelectronic devices.

19972 | *J. Mater. Chem. A*, 2021, **9**, 19965–19974

This journal is © The Royal Society of Chemistry 2021

Conflicts of interest

There are no conflicts to declare.

Acknowledgements

References

1 L. Finegold and J. L. Cude, *Nature*, 1972, **238**, 38–40.

2 C. Jiang, S. J. A. Moniz, A. Wang, T. Zhang and J. Tang, *Chem. Soc. Rev.*, 2017, **46**, 4645–4660.

3 M. Law, L. E. Greene, J. C. Johnson, R. Saykally and P. Yang, *Nat. Mater.*, 2005, **4**, 455–459.

4 J. Du, J. Qi, D. Wang and Z. Tang, *Energy Environ. Sci.*, 2012, **5**, 6914–6918.

5 Y. Bai, I. Mora-Seró, F. De Angelis, J. Bisquert and P. Wang, *Chem. Rev.*, 2014, **114**, 10095–10130.

6 Z. Bai, X. Yan, Y. Li, Z. Kang, S. Cao and Y. Zhang, *Adv. Energy Mater.*, 2016, **6**, 1–8.

7 W. Wang, C. Jin and L. Qi, *Small*, 2018, **14**, 1–10.

8 S. Sahu and S. Chandra, *Sol. Cells*, 1987, **22**, 163–173.

9 W. Li, P. Da, Y. Zhang, Y. Wang, X. Lin, X. Gong and G. Zheng, *ACS Nano*, 2014, **8**, 11770–11777.

10 H. Dotan, K. Sivula, M. Grätzel, A. Rothschild and S. C. Warren, *Energy Environ. Sci.*, 2011, **4**, 958–964.

11 T. Kim and K. Choi, *Science*, 2014, **343**, 990–994.

12 K. T. Fountaine, H. J. Lewerenz and H. A. Atwater, *Nat. Commun.*, 2016, **7**, 1–9.

13 M. Radecka, A. Wnuk, A. Trenczek-Zajac, K. Schneider and K. Zakrzewska, *Int. J. Hydrogen Energy*, 2015, **40**, 841–851.

14 H. Wang, H. Li, S. Cao, M. Wang, J. Chen and Z. Zang, *Sol. RRL*, 2020, **4**, 2000226.

15 X. Hu, H. Wang, M. Wang and Z. Zang, *Sol. Energy*, 2020, **206**, 816–825.

16 S. Cao, H. Wang, H. Li, J. Chen and Z. Zang, *Chem. Eng. J.*, 2020, **394**, 124903.

17 H. Wang, H. Li, W. Cai, P. Zhang, S. Cao, Z. Chen and Z. Zang, *Nanoscale*, 2020, **12**, 14369–14404.

18 H. C. Shin, J. Dong and M. Liu, *Adv. Mater.*, 2004, **16**, 237–240.

19 J. Y. Kim, J. S. Kang, J. Shin, J. Kim, S. J. Han, J. Park, Y. S. Min, M. J. Ko and Y. E. Sung, *Nanoscale*, 2015, **7**, 8368–8377.

20 Z. Zhang, C. Gao, Z. Wu, W. Han, Y. Wang, W. Fu, X. Li and E. Xie, *Nano Energy*, 2016, **19**, 318–327.

21 L. Xiong, Y. Guo, J. Wen, H. Liu, G. Yang, P. Qin and G. Fang, *Adv. Funct. Mater.*, 2018, **28**, 1–18.

22 M. F. Mohamad Noh, N. A. Arzaee, J. Safaei, N. A. Mohamed, H. P. Kim, A. R. Mohd Yusoff, J. Jang and M. A. Mat Teridi, *J. Alloys Compd.*, 2019, **773**, 997–1008.

23 J. Wang, K. Datta, C. H. L. Weijtens, M. M. Wienk and R. A. J. Janssen, *Adv. Funct. Mater.*, 2019, **29**, 1905883.

24 E. Jiang, Y. Ai, J. Yan, N. Li, L. Lin, Z. Wang, C. Shou, B. Yan, Y. Zeng, J. Sheng and J. Ye, *ACS Appl. Mater. Interfaces*, 2019, **11**, 36727–36734.

25 Y. Luan, X. Yi, P. Mao, Y. Wei, J. Zhuang, N. Chen, T. Lin, C. Li and J. Wang, *iScience*, 2019, **16**, 433–441.

26 J. Liang, Z. Chen, G. Yang, H. Wang, F. Ye, C. Tao and G. Fang, *ACS Appl. Mater. Interfaces*, 2019, **11**, 23152–23159.

27 E. Mokaripoor and M. M. Bagheri-Mohagheghi, *Mater. Sci. Semicond. Process.*, 2015, **30**, 400–405.

28 B. Zhang, Y. Tian, J. X. Zhang and W. Cai, *Vacuum*, 2011, **85**, 986–989.

29 T. T. Nguyen, H. P. Dang, Q. H. Luc and T. Le, *Ceram. Int.*, 2019, **45**, 9147–9156.

30 H. Tan, A. Jain, X. Lan, F. P. G. Arquer, J. Z. Fan, R. Quintero-Bermudez, M. Yuan, B. Zhang, Y. Zhao, F. Fan, P. Li, L. N. Quan, Y. Zhao, Z. Lu, Z. Yang, S. Hoogland and E. H. Sargent, *Science*, 2017, **355**, 722–726.

31 P. Karthick, K. Saravanakumar, C. Sanjeeviraja and K. Jeyadheepan, *Thin Solid Films*, 2020, **713**, 138362.

32 J. E. N. Swallow, B. A. D. Williamson, T. J. Whittles, M. Birkett, T. J. Featherstone, N. Peng, A. Abbott, M. Farnworth, K. J. Cheetham, P. Warren, D. O. Scanlon, V. R. Dhanak and T. D. Veal, *Adv. Funct. Mater.*, 2018, **28**, 1–10.

33 A. K. Saxena, R. Thangaraj, S. P. Singh and O. P. Agnihotri, *Bull. Mater. Sci.*, 1986, **8**, 315–318.

34 X. Wang, X. Wang, Q. Di, H. Zhao, B. Liang and J. Yang, *Materials*, 2017, **10**, 1398.

35 H. Wang, K. Dou, W. Y. Teoh, Y. Zhan, T. F. Hung, F. Zhang, J. Xu, R. Zhang and A. L. Rogach, *Adv. Funct. Mater.*, 2013, **23**, 4847–4853.

36 N. Noor, C. K. T. Chew, D. S. Bhachu, M. R. Waugh, C. J. Carmalt and I. P. Parkin, *J. Mater. Chem. C*, 2015, **3**, 9359–9368.

37 N. Noor and I. P. Parkin, *J. Mater. Chem. C*, 2013, **1**, 984–996.

38 J. H. Kim, S. Yonezawa and T. Okada, *Chem. Lett.*, 2018, **47**, 393–395.

39 C. Wyse, R. Torres, T. Barnes, M. Scott, M. Young, X. Li and T. Gessert, *2009 34th IEEE Photovoltaic Specialists Conference (PVSC)*, IEEE, 2009, pp. 002435–002438.

40 T. Jäger, Y. E. Romanyuk, A. N. Tiwari and A. Anders, *J. Appl. Phys.*, 2014, **116**, 033301.

41 Z. Banyamin, P. Kelly, G. West and J. Boardman, *Coatings*, 2014, **4**, 732–746.

42 G. C. Morris and A. E. McElnea, *Appl. Surf. Sci.*, 1996, **92**, 167–170.

43 G. Bahuguna, I. Mondal, M. Verma, M. Kumar, S. Bhattacharya, R. Gupta and G. U. Kulkarni, *ACS Appl. Mater. Interfaces*, 2020, **12**, 37320–37329.

This journal is © The Royal Society of Chemistry 2021

J. Mater. Chem. A, 2021, **9**, 19965–19974 | **19973**

44 G. Bahuguna, S. Chaudhary, R. K. Sharma and R. Gupta, *Energy Technol.*, 2019, **7**, 1–8.

45 M. P. Genovese, I. V. Lightcap and P. V. Kamat, *ACS Nano*, 2012, **6**, 865–872.

46 M. Park, J. Y. Kim, H. J. Son, C. H. Lee, S. S. Jang and M. J. Ko, *Nano Energy*, 2016, **26**, 208–215.

47 V. H. Tran, R. B. Ambade, S. B. Ambade, S. H. Lee and I. H. Lee, *ACS Appl. Mater. Interfaces*, 2017, **9**, 1645–1653.

48 T. Rhimi, M. Toumi, K. Khirouni and S. Guermazi, *J. Alloys Compd.*, 2017, **714**, 546–552.

49 P. V. Bhuvaneswari, P. Velusamy, R. R. Babu, S. M. Babu, K. Ramamurthi and M. Arivanandhan, *Mater. Sci. Semicond. Process.*, 2013, **16**, 1964–1970.

50 S. D. Taylor, C. Christopher and G. Hum, *Tetrahedron*, 1999, **55**, 12431–12477.

51 S. Zhan, D. Li, S. Liang, X. Chen and X. Li, *Sensors*, 2013, **13**, 4378–4389.

52 A. Huda, I. P. Mahendra, R. Ichwani, C. T. Handoko, H. M. Ngoc, B. Yudono, M. D. Bustan and F. Gulo, *Rasayan J. Chem.*, 2019, **12**, 308–318.

53 J. B. Gilbert, M. F. Rubner and R. E. Cohen, *Proc. Natl. Acad. Sci. U. S. A.*, 2013, **110**, 6651–6656.

54 Y. Kang and C. G. Van de Walle, *Appl. Phys. Lett.*, 2017, **111**, 152107.

55 D. R. Acosta, E. P. Zironi, E. Montoya and W. Estrada, *Thin Solid Films*, 1996, **288**, 1–7.

56 M. Kwoka, L. Ottaviano, M. Passacantando, S. Santucci, G. Czempik and J. Szuber, *Thin Solid Films*, 2005, **490**, 36–42.

57 J. Kim, A. Ho-Baillie and S. Huang, *Sol. RRL*, 2019, **3**, 1–16.

58 W. Shen, T. Ou, J. Wang, T. Qin, G. Zhang, X. Zhang, Y. Han, Y. Ma and C. Gao, *Sci. Rep.*, 2018, **8**, 5086.

59 D. K. Bandgar, S. T. Navale, M. Naushad, R. S. Mane, F. J. Stadler and V. B. Patil, *RSC Adv.*, 2015, **5**, 68964–68971.

60 M. A. Ponce, P. R. Bueno, J. Varel, M. S. Castro and C. M. Aldao, *J. Mater. Sci.: Mater. Electron.*, 2008, **19**, 1169–1175.

61 M. Coskun, O. Polat, F. M. Coskun, Z. Durmus, M. Çaglar and A. Turut, *RSC Adv.*, 2018, **8**, 4634.

62 H. Che and M. El Bouanani, *Nucl. Instrum. Methods Phys. Res., Sect. B*, 2018, **414**, 170–175.

63 M. F. Aygüler, A. G. Hufnagel, P. Rieder, M. Wussler, W. Jaegermann, T. Bein, V. Dyakonov, M. L. Petrus, A. Baumann and P. Docampo, *ACS Appl. Mater. Interfaces*, 2018, **10**, 11414–11419.

64 F. Mohamadkhani, S. Javadpour and N. Taghavinia, *Sol. Energy*, 2019, **191**, 647–653.